CrossMark

New Horizons Photometry of Pluto's Moon Charon

B. J. Buratti[1], M. D. Hicks[1], J. H. Hillier[2], A. J. Verbiscer[3] , M. Abgarian[1], J. D. Hofgartner[1], T. R. Lauer[4] , W. M. Grundy[5], S. A. Stern[6], H. A. Weaver[7] , C. J. A. Howett[6], L. A. Young[6], A. Cheng[7], R. A. Beyer[8], C. M. Lisse[7] , K. Ennico[9] , C. B. Olkin[6] , and S. J. Robbins[6]

[1] Jet Propulsion Laboratory, California Institute of Technology, Pasadena, CA 91109, USA; bonnie.buratti@jpl.nasa.gov
[2] Grays Harbor College, Aberdeen, WA 98520, USA
[3] University of Virginia, Charlottesville, VA 22904, USA
[4] NOAO, Tucson, AZ 85726, USA
[5] Lowell Observatory, Flagstaff, AZ 86001, USA
[6] Southwest Research Institute, Boulder, CO 80302, USA
[7] Johns Hopkins University, Applied Physics Laboratory, Laurel, MD 20723, USA
[8] SETI Institute, Mountain View, CA 94043, USA
[9] National Aeronautics and Space Administration (NASA) Ames Research Center, Moffett Field, CA 94035, USA

Abstract

The *New Horizons* spacecraft extended the range in solar phase angle coverage for Pluto's moon Charon from $1°.8$ —the maximum observable from Earth—to $170°$. This extraordinary expansion in range has enabled photometric modeling and a robust determination of Charon's phase integral and Bond albedo at visible wavelengths. Photometric modeling shows that Charon is similar in its photometric properties to other icy moons, except that its single particle phase function is more isotropic, suggesting the Kuiper Belt may represent a new regime for surface alteration processes. Charon's phase integral is 0.70 ± 0.04 and its Bond albedo is 0.29 ± 0.05.

Key words: Kuiper belt: general – Kuiper belt objects: individual (Charon, Pluto) – planets and satellites: surfaces – techniques: photometric

1. Introduction

Quantitative measurements of reflected light from planetary bodies obtained during spacecraft encounters have opened up a whole new way of understanding their surfaces. Models developed originally in the early 1980s that express the intensity returned from planetary surfaces in terms of surface porosity, roughness, component particle sizes, and single scattering albedo have revolutionized our view of the morphology of planets, moons, and small bodies (Horak 1950; Chandrasekhar 1960; Goguen 1981; Hapke 1981, 1984, 1986, 1990, 2008; Buratti 1985). Analysis of a wide variety of objects, including asteroids (e.g., Helfenstein & Veverka 1989; Li et al. 2013), icy and rocky moons (e.g., Verbiscer & Veverka 1989; Domingue et al. 1991; Buratti et al. 2006), Kuiper Belt Objects (Hicks et al. 2005), and comets (Masoumzadeh et al. 2017) has led to an understanding of macroscopic surface roughness and aggregate scattering properties of particles comprising these bodies' surfaces. Although the models have limitations on their physical reality—as all models do—and their uniqueness (see Helfenstein et al. 1988), so many objects have been fit to what are sometimes called "Hapke Models," and thus comparisons among a wide range of objects can be made. The models are based on radiative transfer theory combined with empirical constructs or highly idealized models to represent the physical parameters, some of which Hapke developed. Most significantly, comparative studies of geophysical processes occurring on the surfaces of icy and rocky bodies, from objects in the inner to the outer solar system, encompassing a wide range of compositions and surface temperatures, can be probed.

During the 2015 *New Horizons* encounter with the Pluto system, observations of its main moon Charon were obtained with the full range of remote sensing instruments (Stern et al. 2015). Although photometric observations were concentrated on Pluto, *New Horizons* also obtained a good range of solar phase angle observations of Charon, particularly when one realizes that Earth-based observations of Charon are restricted to solar phase angles $(\alpha) = 1°.8$, and that separate photometric accuracy for both Pluto and Charon requires adaptive optics systems for ground-based telescopes. Thus, the combined data set obtained with the Long-Range Reconnaissance Imager (LORRI; Cheng et al. 2008) and the Multispectral Visible Imaging Camera (MVIC; Reuter et al. 2008) represent an observational treasure.

In this paper we present full-disk solar phase curves of Charon spanning the phase angles $15°–169°.5$ obtained at wavelengths between 0.41 and 0.8 μm. Some of the LORRI observations were not full-disk images, but we were able to obtain equivalent disk-integrated brightnesses with well-established techniques that compute equivalent spheres from partial-disk observations (Buratti & Veverka 1983; Buratti 1984). We combine these data with the small phase angle *Hubble Space Telescope (HST)* observations of Charon (Buie et al. 2010) to fit a radiative transfer model that derives the roughness, porosity, and directional scattering properties of the surface. The physical photometric properties of this medium-sized KBO are the first such published for this class of object based on a large range of solar phase angles, and as such represent the opportunity to compare its properties—and thus its geophysical evolution—to kindred objects. Appearing to have only partly melted and differentiated, Charon is not as physically evolved as Pluto (Stern et al. 2015), although it may not be a good comparator to KBOs formed in the solar nebula as it may have formed in a collision with Pluto (Canup 2005). There are existing near-opposition analyses of Hicks et al. (2005), Rabinowitz et al. (2007), and Buie et al. (2010), and a photometric study of Phoebe, which is likely a captured KBO, with near-IR observations from *Cassini* (Buratti et al. 2008).

Figure 1. Charon, Pluto's main moon. Main vitals are radius: 606 km (Nimmo et al. 2017); rotational period: 6.4 days; primary surface composition: water ice (Grundy et al. 2016a); and bulk density: 1.7 g/cc (Stern et al. 2015). Mordor Macula (the name is informal) is the reddish north polar cap at the top of the image. For a quantitative description of global colors see Olkin et al. (2017).

The large excursion in solar phase angles measured by *New Horizons* also represents an opportunity to derive an accurate and direct measurement of the Bond albedo of Charon, which is key for thermal modeling and understanding volatile transport on its surface (e.g., Grundy et al. 2016b).

2. Data

In the week leading up to the 2015 July *New Horizons* flyby of Pluto and its moon, images at all longitudes of Charon were obtained by the remote sensing instruments on the spacecraft. Closest approach images provided high resolution measurements of only one hemisphere of Pluto and Charon (Figure 1). LORRI and MVIC images obtained in the week leading up to the *New Horizons* closest approach of Pluto thus provided a full rotation light curve for Charon spanning the visible and near-IR.

The MVIC and LORRI images used for constructing the disk-integrated solar phase curves of Charon are described in Table 1, along with their integration times and their associated geometric information including solar phase angle, range, subspacecraft geographical latitude and longitude, and normalized integrated surface phase function. The integration times were 0.59–0.62 s for MVIC and 0.10 or 0.15 s for LORRI. The distance to Charon from the spacecraft ranged from 180,000 to 31,000 km. For most of the data, Pluto and Charon appear on the same image: three days before closest approach the binary pair exceeded the LORRI field of view. Pipeline calibration procedures were employed to flatfield each image, remove blemishes, and transform data numbers into radiometric units using the flight calibration current as of 2016 August. Some of the images are not full-disk, but we derived the equivalent full-disk brightness by the straightforward and well-established technique described below. MVIC images are useful mainly for color light curves, while the LORRI data provide the largest range in solar phase angles for photometric modeling.

The smallest solar phase angle observed by *New Horizons* was 15°. Observations at smaller solar phase angles

encompassing the opposition surge are key to understanding the porosity and mean particle size of grains comprising the regolith (Irvine 1966; Hapke 2008). We therefore folded the *HST* observations of Buie et al. (2010) into our collection to extend the phase angle reach to the opposition region. Although the Buie et al. data are only in the B- and V-filters (0.44 and 0.55 μm), we transform our LORRI data into the V-filter; in any case, the phase angle coverage in LORRI is one of the rare data sets from *New Horizons* sufficient to perform photometric modeling. The LORRI images at 169°5 were especially problematical as substantial scattered light plagued the data. Because these observations doubled the excursion in solar phase angle for our data set, substantial effort was expended in reducing these observations. Scattered light was carefully measured from the residual signal on the background of each image and subtracted, and then all of the images obtained at this solar phase angle were coadded.

3. Analysis

Creation of disk-integrated solar phase curves using aperture photometry is straightforward; the techniques we have used for both Earth-based and spacecraft images have been described (e.g., Buratti & Veverka 1983, 1984; Buratti et al. 2015). After calibration of the images including flat-fielding and subtraction of residual background, the integral brightness of Charon was calculated by coadding all illuminated pixels and correcting to a common spacecraft distance. An important correction is the removal of rotational phase variations, even though it is known that these are not large for Charon (Buie et al. 2010). Generally, we fit the rotational phase curve with a Fourier expansion and a liner solar phase coefficient simultaneously (e.g., Buratti et al. 2015). However, the approach solar phase angle did not change substantially, so we created the solar phase curves with the incoming data and simply corrected the few points at larger phase angles by computing the phase coefficient between these points and their measurements at the same longitude as the approach phase angle. The subobserver latitude during the *New Horizons* encounter was 43°, as compared to 30°–31° at the time the Buie et al. data were obtained. We did not correct for this change.

Key observations that did not include the whole disk of Charon were obtained at larger solar phase angles. It is a relatively straightforward task to create the equivalent disk-integrated measurement by computing a sphere covered by a photometric function defined by the measured I/F. A simple photometric function that has been widely used is the superposition of a lunar, or Lommel–Seeliger law, describing singly scattered radiation, and a Lambert law describing multiple scattered photons (Buratti 1984):

$$\frac{I}{F} = \frac{f(\alpha)A\mu_0}{\mu_0 + \mu} + (1 - A)\mu_0. \tag{1}$$

Here I is the intensity of scattered light at a point on a planetary disk, πF is the incidence solar flux at that point, α is the solar phase angle, μ_0 is the cosine of the incidence angle, μ is the cosine of the emission angle, and A is the fraction of radiation that is singly scattered. The term $f(\alpha)$ is the surface phase function: it expresses changes in the scattering behavior of the surface due to the physical properties of roughness, compaction state, and scattering anisotropy defined above. This equation is

Table 1
Observational Circumstances: Disk-integrated MVIC and LORRI Data

UT (2015)	Sub-SC Long. (°)	Sub-SC Lat. (°)	Solar Phase (°)	#Images (Each Filter)	Normalized Brightness Blue	Normalized Brightness LORRI	Normalized Brightness Red	Normalized Brightness NIR	Normalized Brightness Methane
Jun 6 09:59–Jul 13 07:38	32.7–349.5	42.2–43.2	14.9–15.6	19-52-22-13-21	0.984 ± 0.010	0.980 ± 0.008	0.972 ± 0.017	0.990 ± 0.006	0.982 ± 0.009
Jul 13 14:50	16.2	42.0	16.1	1-1-1-1-1	0.982 ± 0.010	0.975 ± 0.008	0.969 ± 0.017	0.987 ± 0.006	0.978 ± 0.009
Jul 13 21:08	2.1	41.5	16.8	1-3-1-1-1	0.985 ± 0.010	0.972 ± 0.008	0.930 ± 0.017	⋯	0.974 ± 0.009
Jul 14 02:47	350.2	40.5	18.3	1-4-1-1-1	0.970 ± 0.010	0.951 ± 0.008	0.918 ± 0.017	0.927 ± 0.006	0.938 ± 0.009
Jul 14 06:50	343.3	38.5	21.1	1-0-1-1-1	0.898 ± 0.010	⋯	0.850 ± 0.017	0.887 ± 0.006	0.868 ± 0.009
Jul 14 19:44	123.3	−45.6	169.5	0-1-0-0-0	⋯	$3.0 \pm 0.2 \times 10^{-5}$	⋯	⋯	⋯

only semi-empirical, as it contains the leading terms of more complete equations of radiative transfer (Goguen 1981).

For Charon, we find that $A = 0.9$ is a good fit, and is in agreement with previous results on icy moons (Buratti 1984). If a spherical planetary body obeys the photometric function described above, its normalized disk-integrated brightness Φ is given by:

$$\Phi(\alpha) = \{2/3(1 - A)(\sin\alpha + (\pi - \alpha)\cos\alpha) \\ + Af(\alpha)\pi/2[1 - \sin(\alpha/2)\tan(\alpha/2)\ln\cot(\alpha/4)]\}/\pi \\ \times [(2/3)(1 - A) + Af(0°)/2]. \tag{2}$$

(In Buratti & Veverka 1983, there should be a π in the denominator, and in Buratti (1984) the $f(0°)$ should be divided by 2.) To compute the I/F values, we centroided the illuminated portion of Charon and an aperture of 50 pixel radius was defined and averaged. The $f(\alpha)$s were computed from Equation (1) and the surface phase function at $f(0°)$ was calculated from the geometric albedo p, given by (Buratti & Veverka 1983):

$$p = 2/3(l - A) + Af(0°)/2. \tag{3}$$

The geometric albedo for Charon was already derived to be 0.41 in the V-filter (Buratti et al. 2017). For each disk-resolved image, an average $f(\alpha)$ was computed after correcting for variations due to changes in emission and incidence angle ("limb darkening") employing Equation (1). These values are listed in Table 1.

4. Results

Figure 2(a) shows the rotational light curves created from the approach images for LORRI and four MVIC color filter passbands. The MVIC results are in close agreement with those of Howett et al. (2017). The closest filter to the Earth-based V-measurements in wavelength is the MVIC Blue filter, and it shows fair agreement with Earth-based observations (Buie et al. 2010). We attribute the dip shortward of 300° in the *New Horizons* data to the different subobserver latitudes: the spacecraft gave a more favorable view to the lower albedo, reddish Mordor Macula. Indeed, the red filter shows even better agreement with the Buie et al. data, as Mordor Macula is relatively bright in that filter. One possible implication of these light curves is that they may show the existence of cold-trapped methane. The methane band shows a decreased value, i.e., higher absorption, where the light curve of Charon is at a minimum, the location at which Mordor Macula is most visible. This decrease may be simply an albedo variation (and a fuller analysis convolving the shape of the methane spectrum with the spectral response of the filter is required), but it occurs at the location where cold-trapping of methane is key to the formation of the low-albedo reddish hydrocarbons at Charon's red polar cap (Grundy et al. 2016b).

The solar phase curves corrected for rotational variations are shown in Figure 2(b) (MVIC) and Figure 2(c) (LORRI), which includes the disk-resolved images between 23° and 84°, and the observation at 169°.5. Figure 2(d) shows the phase curve compared with a wide range of solar system airless bodies. Charon's curve is similar to icy moons with comparable or slightly lower albedos—Ganymede and the Uranian moons for example.

The wide excursion in Charon's integral solar phase curve enables the direct measurement of its Bond albedo. And since our phase curve is acquired in the visible filter near the peak of solar radiation, it is close to the bolometric Bond albedo. The Bond albedo is the product of the geometric albedo and the phase integral, q, which expresses the directional scattering properties of a planetary body and is given by:

$$q(\lambda) = 2\int_0^\pi \Phi(\alpha, \lambda)\sin\alpha \, d\alpha, \tag{4}$$

where $\Phi(\lambda)$ is the disk-integrated normalized phase curve. The Bond albedo is a fundamental parameter for understanding energy balance and volatile transport on any planetary surface. Using a four-point Gaussian quadrature formula (Chandrasekhar 1960), interpolating between the points less than 85°, and using Dione's phase curve for values between 85° and 170°, we find a phase integral of 0.70 ± 0.04 and a Bond albedo of 0.29 ± 0.05 using the geometric albedo of 0.41 (Buratti et al. 2017). The result for q is in line with the expectations derived for other icy moons: Rhea and Dione have similar values with 0.63–0.70 and 0.70–0.80, respectively (Buratti & Veverka 1984; Verbiscer et al. 2007, 2013); Europa's is 0.69–1.09 (Buratti & Veverka 1983; Verbiscer et al. 2013); and the Moon's is 0.6 (Lane & Irvine 1973).

5. Photometric Modeling

Equation (1) represents a semi-empirical photometric model that incorporates all the physical parameters into the surface phase function and is useful mainly for practical purposes such as constructing albedo maps (Buratti et al. 2017; Hofgartner et al. 2018) and integral phase curves as described above. A full photometric model is summarized by the following expression for the reflectance r (Horak 1950; Chandrasekhar 1960; Goguen 1981; Hapke 1981, 1984, 1986, 1990, 2008):

$$r(i, e, \alpha) = w/4(\mu_0/(\mu_0 + \mu)([1 + B(\alpha, h, B_0)]P(\alpha) \\ + [H(\mu_0, w)H(\mu, w) - 1])S(i, e, \alpha), \tag{5}$$

where w is the single scattering albedo (the probability that a photon reflected from the surface will be scattered into 2π steradians of space), B is the function representing the opposition surge (h and B_0 describe the shape and amplitude of the surge, which are related to the compaction state), $P(\alpha)$ is the single particle phase function, $H(\mu_0, w)$ and $H(\mu, w)$ are Chandrasekhar's multiple scattering H-functions (Chandrasekhar 1960), and $S(i, e, \alpha)$ is the function describing macroscopic roughness. Here we approximate the roughness parameter by a Gaussian mean slope value, theta-bar (Hapke 1984). The single particle phase function is usually described by a 1 or 2 term Henyey–Greenstein phase function defined by g, where $g = 1$ is purely forward scattering, $g = -1$ is purely backscattering, and $g = 0$ is isotropic.

For a collection of uniform particles with no multiple scattering, h due to shadow hiding is equal to $-(3/8)\ln(1 - \rho/\rho_0)$, where ρ is the bulk density of the regolith particles and ρ_0 is the density of an individual particle and the term in parentheses is the porosity, the fraction of space not occupied by particles or the "void space" (Hapke 1986). The amplitude B_0 is a measure of the opacity of individual particles: for $B_0 = 1$ (the highest value in Hapke's current model) all
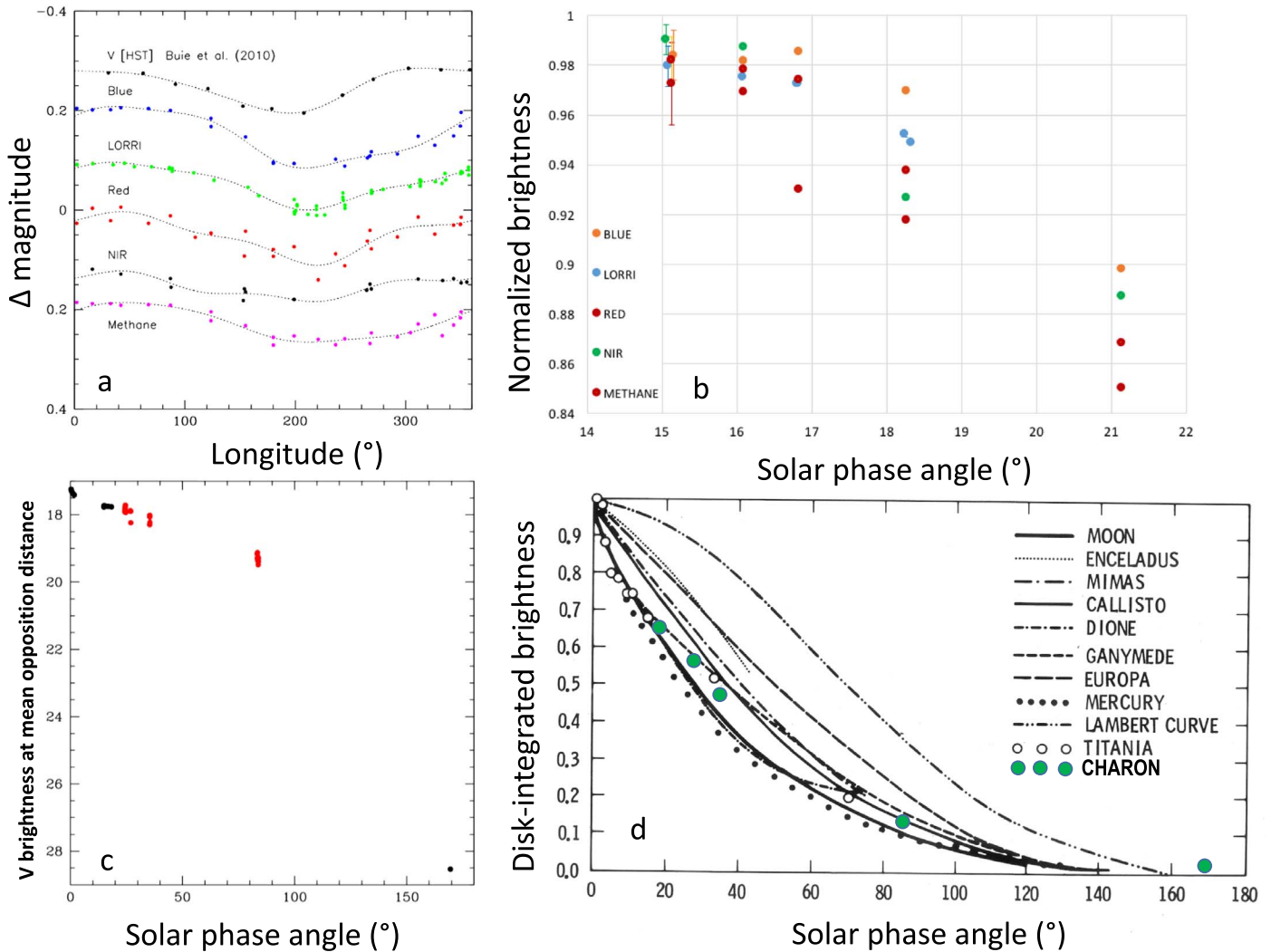
Figure 2. (a) The rotational light curves of Charon in MVIC and LORRI filters corrected to 15°3, shown with *HST* data corrected to 1° (Buie et al. 2010) for comparison. The bandpasses for MVIC in nanometers are Blue: 400–550; Red: 540–700; Near Infrared (NIR): 780–975; and Methane: 860–910. LORRI's broadband filter is centered at 610 nm. MVIC Red and LORRI show good agreement. (b) The MVIC rotation-corrected solar phase curve. The points are normalized to the brightest point in each filter's data set (the final values at each solar phase angle were averaged, so the value closest to 0 is below unity). The typical error is shown in the data at 15°3. (c) The LORRI and Buie et al. (2010) rotation-corrected solar phase curve. The black points are disk-integrated *HST* data (at the very small solar phase angles) and LORRI data, while the red points represent disk-resolved measurements that were converted to disk-integrated measurements as described in the text. Realistic errors are shown by the scatter in the data at each phase angle. (d) The phase curve of Charon compared to various other relevant solar system objects (Base figure is from Buratti et al. 2017).

Table 2
Observational Circumstances: Disk-resolved LORRI Data

UT (2015)	Sub-spacecraft Long. (°)	Sub-spacecraft Lat. (°)	Solar Phase (°)	Num. Images	$\langle \Phi(\alpha) \rangle$	$\langle V_{opp} \rangle$ (mag)	$\langle f(\alpha) \rangle$
Jul 14 08:35	342.0	36.8	24.4	0-8-0-0-0	0.678 ± 0.054	18.040 ± 0.086	0.537 ± 0.055
Jul 14 09:18	342.3	34.2	26.8	0-4-0-0-0	0.591 ± 0.087	18.196 ± 0.173	0.459 ± 0.090
Jul 14 10:29	346.0	27.7	35.4	0-4-0-0-0	0.502 ± 0.061	18.369 ± 0.133	0.407 ± 0.068
Jul 14 11:49	11.3	−12.1	83.5	0-8-0-0-0	0.175 ± 0.019	19.515 ± 0.118	0.243 ± 0.039

impingent radiation is scattered from the front surface of particles with no internal scattering.

The range in solar phase angles for the LORRI data is sufficient to derive photometric parameters. Following the techniques we have used in the past (e.g., Hillier et al. 1999) we find the parameters listed in Tables 2 and 3, and present some kindred objects for comparison. Figure 3 shows the LORRI

data plotted with the model. One important concern is that the number of points at large solar phase angles (>80° or so), where the effects of roughness are most pronounced, may not constrain our value for the slope angle very well. Figure 3 includes several curves over a range of slope angles, illustrating that our fit is reasonable, and a clear best fit for the two observations at the highest solar phase angles.

Table 3
Photometric Modeling of Selected Objects in Comparison to Charon

Object	w	g	Slope Angle θ (°)	h (s)[a]	h (c)[a]	B_o (s)[a]	B_o (c)[a]	Source
Charon	0.72	−0.09	23	0.150	0.037	0.001	0.536	This study
Phoebe	0.07	−0.20	33	0.04	⋯	>1.0	⋯	Simonelli et al. (1999), Buratti et al. (2008)
Nix	0.86	0.49	20[b]	0.50	0.019	0.94	0.87	Verbiscer et al. (2018)
Hydra	0.95	0.44	20[b]	0.16	0.0043	0.88	0.45	Verbiscer et al. (2018)
Rhea	0.861	−0.29	13 ± 5	0.08	⋯	1.37	⋯	Verbiscer & Veverka (1989)
	0.989	0.2	33	0.0004	⋯	1.8	⋯	Ciarniello et al. (2011)
Europa	0.964	−0.15 ± 0.04	10	0.0016	⋯	0.5	⋯	Buratti (1985), Domingue et al. (1991)
C-asteroids	0.037	−0.47	20[b]	0.025	⋯	1.03	⋯	Helfenstein & Veverka (1989)
S-asteroids	0.23	−0.27	20[b]	0.08	⋯	1.60	⋯	Helfenstein & Veverka (1989)
Moon	0.25	−0.25	20	0.05	⋯	1.0	⋯	Buratti (1985), Hillier et al. (1999)
Vesta	0.49	−0.23	8	0.076	⋯	1.66	⋯	Li et al. (2013)

Notes.
[a] Hapke's later models have separate parameters for the shadow hiding and coherent backscatter portions of the opposition surge.
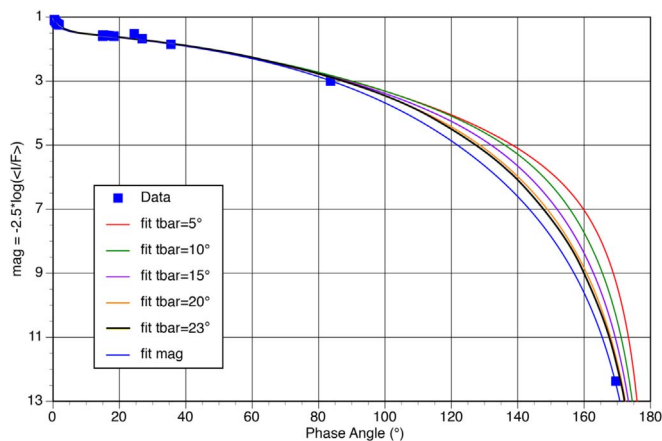[b] Assumed.

Figure 3. LORRI and Earth-based data with the best-fit Hapke model (black line). Models with various mean slope angles (fit tbar) are shown; the best fit is 23°.

6. Discussion

With their vast expansions of the possible viewing geometries of planetary surfaces, spacecraft missions have opened new opportunities for photometric modeling. One of the key findings in early photometric studies was that airless rocky and icy bodies behaved similarly (Buratti 1985). The exploration of the Pluto-Charon system has extended these studies to the edge of the solar system, with the suggestion that surfaces with other ices may show similar morphologies as well (photometric modeling of Pluto's surface is complicated by its atmosphere and is ongoing). Although photometric models are plagued by the lack of uniqueness in their fits (e.g., Helfenstein et al. 1988), by their inexact description of physical reality, and by the updates and alterations being made to the models (e.g., Hapke 2008, 2012), with the fitting of many objects, some comparisons can be made. Tables 2 and 3 suggest that the main differences between Charon and other small bodies in the solar system are in the opposition surge, but since these models have been changing with time, along with the definitions of B_o and h, not too much should be made of this result.

The most interesting result is that the single particle phase function of Charon is more isotropic than other icy bodies, even more so than Europa. Clearly, there is some process occurring on the surface of Charon that "isotropizes" the surface. Grundy et al. (2016b) posit that methane escaping from the atmosphere of Pluto is cold-trapped onto this moon's surface and photolyzed. Although the photolysis processing takes place preferentially at Charon's reddish pole because the methane is thermally stable there, the accretion of atmosphere from Pluto affects the surface globally. The "fluffy" texture may be the result. The drawback to this hypothesis is that the methane is not stable and does not collect anywhere except at the poles. Verbiscer et al. (2018) found that Nix and Hydra are forward scattering, and a reanalysis of Rhea's solar phase curve by Ciarniello et al. (2011) based on *Cassini* data suggests it may also be forward scattering. Charon has its own unique scattering fingerprint, illustrating that it has undergone a unique set of processes that have determined its surface microstructure. As more objects in the Kuiper Belt are explored and modeled, the key question as to whether their surface properties are like the rocky bodies in the inner solar system, the icy bodies around the gaseous planets, or entirely different, as the single particle phase functions of Charon, Nix, and Hydra seem to suggest, will be answered. Phoebe may also be a medium-sized KBO, but its surface properties are more akin to icy moons and the Earth's Moon. This point suggests its exposure to the same conditions as other icy moons— interactions with the solar wind and a similar impact flux, for example—may have led to these similarities.

Charon's surface temperature is colder than that of any previously explored icy world other than Triton, so another possibility is that the very low temperatures result in distinct textures from impact gardening compared with the icy moons of the giant planets. Typical micrometeorite impact speeds will also be considerably lower in the Pluto system, since there is no nearby giant planet to provide gravitational focusing.

In contrast to the results just discussed, the roughness of Charon seems to be in line with other icy moons. However, the images at large solar phase angles are vexed by scattered light and may make this result not entirely robust. And of course no additional solar phase angles can be acquired before a new spacecraft mission is sent to the Pluto system.

One data set that will be available soon, and which will be useful for photometric modeling, is measurements of Pluto and Charon at very small solar phase angles. The system reached a 161 yr low in 2018 (at 0°0061) and the other hemisphere (the side with Tombaugh Regio) will reach a low of 0°016 in 2019. Separate photometric measurements of Pluto and Charon were

made with Earth-based adaptive optics systems (Buratti et al. 2019) and with *HST*.

ORCID iDs

A. J. Verbiscer ⬤ https://orcid.org/0000-0002-3323-9304
T. R. Lauer ⬤ https://orcid.org/0000-0003-3234-7247
H. A. Weaver ⬤ https://orcid.org/0000-0003-0951-7762
C. M. Lisse ⬤ https://orcid.org/0000-0002-9548-1526
K. Ennico ⬤ https://orcid.org/0000-0002-8847-8492
C. B. Olkin ⬤ https://orcid.org/0000-0002-5846-716X

References

Buie, M. W., Grundy, W. M., Young, E. F., et al. 2010, AJ, 139, 1117
Buratti, B. J. 1984, Icar, 59, 392
Buratti, B. J. 1985, Icar, 61, 208
Buratti, B. J., Hicks, M. D., Dalba, P. A., et al. 2015, ApJL, 804, L6
Buratti, B. J., Hicks, M. D., Kramer, E., et al. 2019, LPSC, 50, 1723
Buratti, B. J., Hofgartner, J. D., Hicks, M. D., et al. 2017, Icar, 287, 207
Buratti, B. J., Soderlund, K., Bauer, J., et al. 2008, Icar, 193, 309
Buratti, B. J., Sotin, C., Brown, R. H., et al. 2006, P&SS, 54, 1498
Buratti, B. J., & Veverka, J. 1983, Icar, 55, 93
Buratti, B. J., & Veverka, J. 1984, Icar, 58, 264
Canup, R. M. A. 2005, Sci, 307, 546
Chandrasekhar, S. 1960, Radiative Transfer (New York: Dover)
Cheng, A. F., Weaver, H. A., Conrad, S. J., et al. 2008, SSRv, 140, 189
Ciarniello, M., Capaccioni, F., Filacchione, G., et al. 2011, Icar, 214, 541
Domingue, D. l., Hapke, B., Lockwood, G. W., et al. 1991, Icar, 90, 30
Goguen, J. D. 1981, PhD thesis, Cornell Univ.
Grundy, W., Binzel, R. P., Buratti, B. J., et al. 2016a, Sci, 351, aad9189
Grundy, W., Cruikshank, D. P., Gladstone, G. R., et al. 2016b, Natur, 539, 65
Hapke, B. 1981, JGR, 86, 3039
Hapke, B. 1984, Icar, 59, 41
Hapke, B. 1986, Icar, 67, 264
Hapke, B. 1990, Icar, 88, 407
Hapke, B. 2008, Icar, 195, 918
Hapke, B. 2012, Icar, 221, 1079
Helfenstein, P., & Veverka, J. 1989, in Asteroids II, ed. R. Binzel, T. Gehrels, & M. S. Matthews (Tucson: Univ. Arizona Press)
Helfenstein, P., Veverka, J., & Thomas, P. C. 1988, Icar, 74, 231
Hicks, M. D., Simonelli, D. P., & Buratti, B. J. 2005, Icar, 176, 492
Hillier, J. K., Buratti, B. J., & Hill, K. 1999, Icar, 141, 205
Hofgartner, J. D., Buratti, B. J., Devins, S. L., et al. 2018, Icar, 302, 273
Horak, H. 1950, AJ, 112, 445
Howett, C. J. A., Ennico, K., Olkin, C. B., et al. 2017, Icar, 287, 152
Irvine, W. M. 1966, JGR, 71, 2931
Lane, A. P., & Irvine, W. M. 1973, AJ, 78, 267
Li, J.-Y., Le Corre, L., Schröder, S. E., et al. 2013, Icar, 226, 1252
Masoumzadeh, N., Oklay, N., Kolokolava, L., et al. 2017, A&A, 599, A11
Nimmo, F., Umurhan, O., Lisse, C. M., et al. 2017, Icar, 287, 12
Olkin, C. B., Spencer, J. B., Grundy, G. M., et al. 2017, AJ, 154, 258
Rabinowitz, D., Schaefer, B. E., & Tourtellotte, S. W. 2007, AJ, 133, 26
Reuter, D. C., Stern, S. A., Scherrer, J., et al. 2008, SSRv, 140, 129
Simonelli, D. P., Kay, J., Adinolfi, D., et al. 1999, Icar, 138, 249
Stern, S. A., Bagenal, F., Ennico, K., et al. 2015, Sci, 350, 292
Verbiscer, A., French, R., Showalter, M., et al. 2007, Sci, 315, 815
Verbiscer, A., Helfenstein, P., & Buratti, B. J. 2013, in Europa, ed. M. Gudipati & J. Castillo-Rogez (Berlin: Springer)
Verbiscer, A., Porter, S. B., Buratti, B. J., et al. 2018, ApJL, 852, L35
Verbiscer, A., & Veverka, J. 1989, Icar, 82, 336